

pubs.acs.org/JPCL Letter

# Effect of the Time Delay between Spin State Preparation and Measurement on Electron Spin Teleportation in a Covalent Donor–Acceptor–Radical System

Laura Bancroft, Yunfan Qiu, Matthew D. Krzyaniak,\* and Michael R. Wasielewski\*



Cite This: J. Phys. Chem. Lett. 2022, 13, 156–160



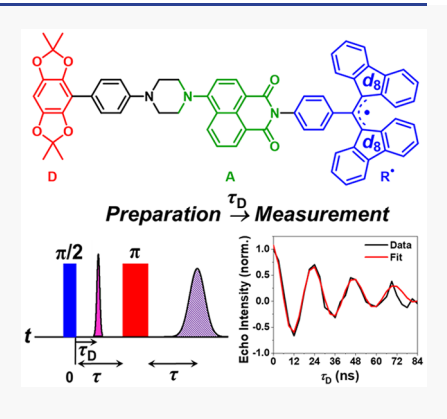
**ACCESS** I

Metrics & More

Article Recommendations

Supporting Information

**ABSTRACT:** We recently demonstrated photodriven quantum teleportation of an electron spin state in a covalent donor—acceptor—radical (D–A–R $^{\bullet}$ ) system. Following specific spin state preparation on R $^{\bullet}$  with a microwave pulse, photoexcitation of A results in two-step electron transfer producing D $^{\bullet+}$ –A–R $^-$ , where the spin state on R $^{\bullet}$  is teleported to D $^{\bullet+}$ . This study examines the effects of varying the time ( $\tau_D$ ) between spin state preparation and photoinitiated teleportation. Using pulse electron paramagnetic resonance spectroscopy, the spin echo of D $^{\bullet+}$  resulting from teleportation shows a damped oscillation as a function of  $\tau_D$  that is simulated using a density matrix model, which provides a fundamental understanding of the echo behavior. Teleportation fidelity calculations also show oscillatory behavior as a function of  $\tau_D$  due to the accumulation of a phase factor between  $\langle S_x \rangle$  and  $\langle S_y \rangle$ . Understanding experimental parameters intrinsic to quantum teleportation in molecular systems is crucial to leveraging this phenomenon for quantum information applications.



ransferring a quantum state over an arbitrary distance from one location to another without destroying the information it contains is possible through the agency of quantum entanglement. The process is known as quantum teleportation<sup>2</sup> and has been demonstrated using both light and matter.3-11 Recently, we achieved electron spin state teleportation in an ensemble of covalent organic donoracceptor-stable radical molecules comprising a 2,2,6,6tetramethylbenzo[1,2-d:4,5-d']bis([1,3]dioxole) donor (D), a 4-aminonaphthalene-1,8-imide acceptor/chromophore (A), and a partly deuterated  $\alpha, \gamma$ -bisdiphenylene- $\beta$ -phenylallyl radical (R\*) [D-A-R\* (Figure 1)]. Following preparation of a specific electron spin state on R o in a magnetic field using a microwave pulse, photoexcitation of A results in the formation of an entangled electron spin pair (D\*+-A\*-). The spontaneous ultrafast electron transfer reaction D\*+-A\*--R\*  $\rightarrow$  D<sup>•+</sup>-A-R<sup>-</sup> constitutes the Bell state<sup>13</sup> measurement step necessary to carry out spin state teleportation. Quantum state

In our previous work, we noted that a phase coherent rotation of the electron spin state teleported to  $D^{\bullet+}$  occurs when the time interval between the initial  $\pi/2$  microwave pulse that places  $R^{\bullet}$  into a superposition state and the laser pulse that initiates teleportation is varied. A better understanding of this observation and how it relates to the teleportation fidelity will inform both future expresimental and malegular design.

tomography of the R<sup>o</sup> and D<sup>o+</sup> spin states using pulse electron

paramagnetic resonance (EPR) spectroscopy showed that the

spin state of R<sup>•</sup> is teleported to D<sup>•+</sup> with ~90% fidelity.

initiates teleportation is varied. A better understanding of this observation and how it relates to the teleportation fidelity will inform both future experimental and molecular design. Utilizing the D-A-R $^{\bullet}$  molecule shown in Figure 1, we observe a damped oscillation of the teleported state when the time between the initial  $\pi/2$  microwave pulse and the laser pulse is incremented. By simulating this behavior using density matrix methods, we show that it is a consequence of the differing resonant frequencies and magnetic environments of R $^{\bullet}$  and D $^{\bullet+}$ .

The synthesis, structural characterization, photoinduced charge separation dynamics, and full quantum state tomography (QST) of teleportation in D-A-R<sup>•</sup> have been described elsewhere. Briefly, following photoexcitation of A, the triradical D<sup>•+</sup>-A<sup>•-</sup>-R<sup>•</sup> is formed in 10 ps. Given that the

 $\begin{array}{c|c} & & & & \\ & & & & \\ & & & & \\ & & \\ & & & \\ & & & \\ & & \\ & & & \\ & & & \\ & & & \\ & & & \\ & & & \\ & & & \\ & & & \\ & &$ 

Figure 1. Structure of D-A-R\*.

Received: November 18, 2021 Accepted: December 22, 2021 Published: December 28, 2021





spins of  $A^{\bullet-}$  and  $R^{\bullet}$  are uncorrelated, the  $D^{\bullet+}-^1(A^{\bullet-}-R^{\bullet}) \to D^{\bullet+}-A-R^-$  reaction occurs in 108 ps with a 25% yield, while the  $D^{\bullet+}-^3(A^{\bullet-}-R^{\bullet}) \to D-A-R^{\bullet}$  reaction occurs in 5 ns with a 75% yield.

Partial QST was performed for teleportation of the +x prepared state using the two- and three-pulse, two-frequency experiments as a function of the time between the initial  $\pi/2$  microwave pulse and the laser pulse,  $\tau_{\rm D}$  (Figure 2). The phase

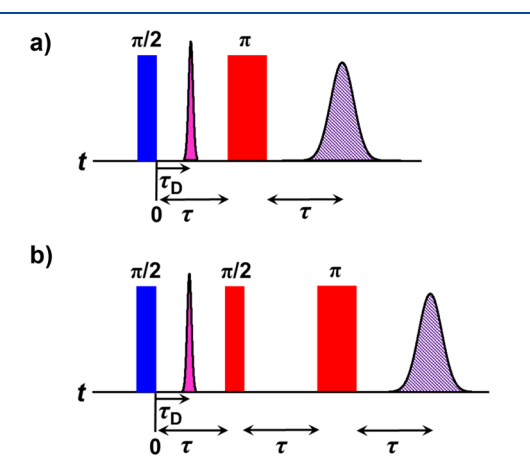


Figure 2. Microwave and laser pulse sequences for (a) two-pulse and (b) three-pulse teleportation experiments in which the laser pulse is delayed by  $\tau_{\rm D}$  relative to the initial  $\pi/2$  microwave pulse. Blue rectangles signify microwave pulses resonant with R $^{\bullet}$ , and red rectangles signify microwave pulses resonant with D $^{\bullet+}$ . Purple spikes signify the 416 nm laser pulse. Pulse turning angles are given above each pulse. The interpulse spacing of the microwave pulses is 200 ns.

cycles used in all experiments are listed in Table S4. The data were collected in triplicate on three separate days with three separate samples. Additional experimental parameters for the triplicate data sets are listed in Table S5.

Figure 3 shows the QST of a state prepared along the +x direction of the Bloch sphere as a function of  $\tau_D$  for data set 1. The two-pulse teleportation experiment (Figure 3a,b) provides  $\langle S_x \rangle$  and  $\langle S_y \rangle$  from the in-phase and quadrature channels of the EPR spectrometer. A damped oscillation of the spin echo intensity is observed as  $\tau_D$  is incremented to longer values, where the amplitude oscillates between  $\langle S_x \rangle$  and  $\langle S_y \rangle$ . In addition, the spin echo moves closer in time to the  $\pi$  microwave pulse with an increase in  $\tau_D$ . As expected, the three-

pulse teleportation experiment, which provides  $\langle S_z \rangle$ , shows no spin echo (Figure 3c).

Fitting a line across the echo maxima and minima in the  $\langle S_x \rangle$  data (Figure 4a) gives a data slice (Figure 4b) that emphasizes the oscillatory and damping behavior of the echo. A fit to the data slice using an exponentially damped sine wave yields a frequency and a decay lifetime, which averaged over the three data sets gives values of 42.2  $\pm$  0.7 MHz and 38  $\pm$  3 ns, respectively. The oscillation frequencies and decay lifetimes from fitting the individual data sets are listed in Table S1. Additional fitting details are also provided in Section 3 of the Supporting Information.

The two-pulse echo versus  $\tau_{\rm D}$  spectra were simulated by evolution of the density matrix. Due to the fast charge separation sequence  ${\rm D}^{-1}*{\rm A}-{\rm R}^{\bullet}\to {\rm D}^{\bullet+}-{\rm I}({\rm A}^{\bullet-}-{\rm R}^{\bullet})\to {\rm D}^{\bullet+}-{\rm A}-{\rm R}^{-}$ , the evolution of the density matrix can be divided into two discrete  $S={}^1/{}_2$  evolution periods, one before the laser pulse and one after it, greatly simplifying the analysis compared to previous treatments. On the basis of the fact that the spins on  ${\rm A}^{\bullet-}$  and  ${\rm R}^{\bullet}$  are uncorrelated, the corresponding triplet intermediate  ${\rm D}^{\bullet+}-{\rm I}({\rm A}^{\bullet-}-{\rm R}^{\bullet})$ , which constitutes 75% of the total triradical intermediate population, decays to  ${\rm D}-{\rm A}-{\rm R}^{\bullet}$  in 5 ns and thus can be safely neglected.

Initially, the thermal density matrix for each  $R^{\bullet}$  spin packet is rotated by the initial  $\pi/2$  microwave pulse generating the +x state. This density matrix then evolves for time  $\tau_{\rm D}$ , acquiring a phase of  ${\rm e}^{i(\omega_{\rm R}+\Delta\omega_{\rm R})\tau_{\rm D}}$ , where  $\omega_{\rm R}$  is the resonant frequency of  $R^{\bullet}$  and  $\Delta\omega_{\rm R}$  represents the offset of the individual spin packets. Following the teleportation event, the density matrix begins evolving under the  $D^{\bullet+}$  spin Hamiltonian adding an addition phase of  ${\rm e}^{i(\omega_{\rm D}+\Delta\omega_{\rm D})(\tau-\tau_{\rm D})}$ , where  $\omega_{\rm D}$  is the resonant frequency of  $D^{\bullet+}$  and  $\Delta\omega_{\rm D}$  represents the offset of the individual spin packets, which are uncorrelated with those of  $R^{\bullet}$ . The spin ensemble described by this density matrix is then refocused with a  $\pi$  microwave pulse resonant with  $D^{\bullet+}$ , subtracting a phase of  ${\rm e}^{i(\omega_{\rm D}+\Delta\omega_{\rm D})\tau}$  and forming a spin echo. The spin echo carries the residual phase of  ${\rm e}^{i(\omega_{\rm R}+\Delta\omega_{\rm R})\tau_{\rm D}-(\omega_{\rm D}+\Delta\omega_{\rm D})\tau_{\rm D}}$ .

The density matrix simulation was coded in Matlab, <sup>18</sup> and the spin echo was generated using the Easyspin <sup>19</sup> function *evolve*. The simulations used the *g* values and line widths determined previously for both R<sup>•</sup> and D<sup>•+</sup>. <sup>12</sup> Integration over the spin packet distributions utilized 30 evenly spaced frequency points in the R<sup>•</sup> spectrum over 45 MHz and 1024 evenly spaced frequency points over 100 MHz in the D<sup>•+</sup> spectrum. Specific frequency ranges were chosen to symmetri-

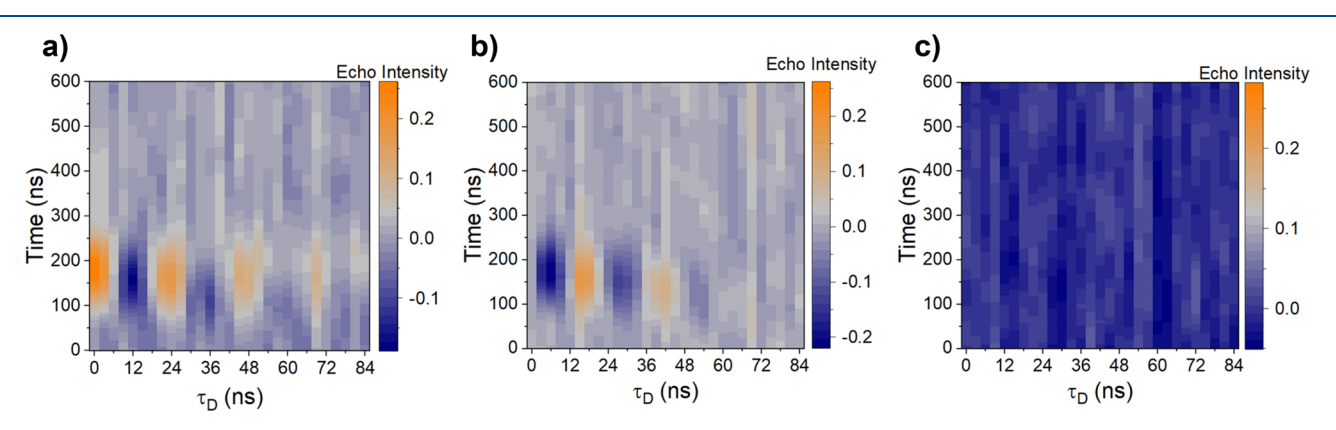
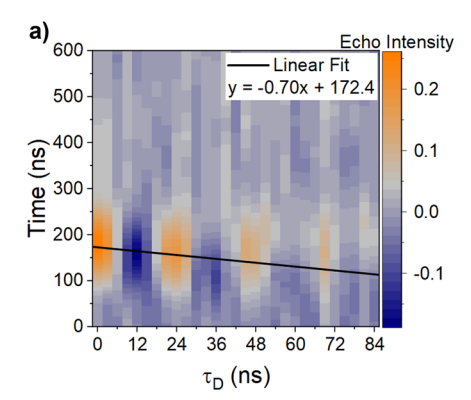


Figure 3. Spin echoes as a function of  $\tau_D$ , which represent the measurement of (a)  $\langle S_x \rangle$ , (b)  $\langle S_y \rangle$ , and (c)  $\langle S_z \rangle$  of a state prepared along the +x direction. Data for panels a and b were collected using the two-pulse teleportation scheme, and data for panel c using the three-pulse scheme. The y-axis is the time after the  $\pi$  microwave pulse. All three panels are from data set 1.



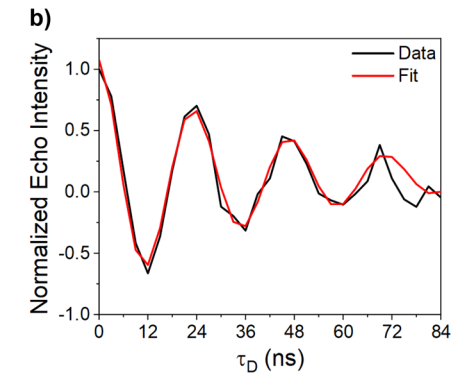


Figure 4. (a) Data for  $\langle S_x \rangle$  with a linear fit across echo maxima and minima. The y-axis is the time after the  $\pi$  microwave pulse. (b) Data slice with corresponding sinusoidal and exponential fits. Both panels are for data set 1.

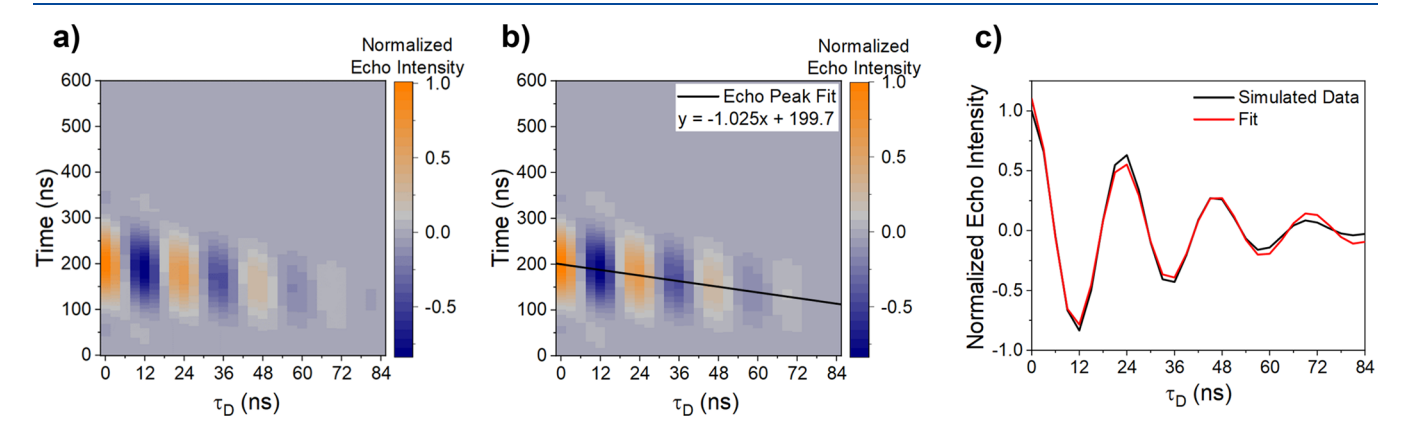


Figure 5. (a) Simulated spin echoes as a function of  $\tau_D$ , which represent the  $\langle S_x \rangle$  measurement of a state prepared along the +x direction. (b) Simulated spin echoes with a linear fit across the echo maxima and minima. The y-axis in panels a and b is the time after the  $\pi$  microwave pulse. (c) Data slice along the linear fit with a corresponding fit. Simulations were generated using the experimental parameters from data set 1.

cally capture the entirety of each spectrum. Experimental microwave pulse lengths, rectangular pulse shapes, and phase cycles were also incorporated into the numerical simulations for each experimental data set.

The simulation of the two-pulse teleportation experiment as a function of  $\tau_{\rm D}$  is shown in Figure 5a. Qualitatively, the simulation agrees well with the experimental results, showing a damped oscillation. A linear fit (Figure 5b) and a data slice (Figure 5c) were obtained in the same manner as the experimental data. The fit of all simulated data sets, as shown for data set 1 in Figure 5c, with the same model as the experimental data yields an average frequency of 42.2 MHz and an average decay lifetime of 35.6 ns. The oscillation frequencies and decay lifetimes from fitting the simulations of the individual data sets are listed in Table S2.

The teleportation fidelity  $F(\rho, \sigma)$ , where  $0 \le F \le 1$ , was calculated as a function of  $\tau_{\rm D}$  using the well-known density matrix expression shown in eq 1.<sup>10,12,20</sup>

$$F(\rho, \sigma) \equiv \left(tr\sqrt{\rho^{1/2}\sigma\rho^{1/2}}\right)^2 \tag{1}$$

where  $\rho$  and  $\sigma$  are density matrices for the starting and final spin states, respectively. The previously reported entanglement fidelity of 0.91 was used, and the values for the input density matrix were replaced with an idealized input density matrix for which F=1. Our previously reported experimental input fidelity of 0.99 suggests that this change should not influence the fidelity calculation, and the idealized input

density matrix will allow an accurate comparison of teleportation fidelities as a function of  $\tau_D$ .

The teleportation fidelity data as a function of  $\tau_{\rm D}$  were fit to extract an oscillation frequency from each data set. The fit protocol involved a sine wave to capture the oscillations and an exponential component to capture the shallower troughs particularly for data sets 2 and 3 (see the Supporting Information). The teleportation fidelity was calculated as a function of  $\tau_{\rm D}$ , and these data are presented in Figure 6 for data set 1. The fidelity oscillates with an average frequency for the triplicate data sets of 41  $\pm$  2 MHz. Each peak returns to roughly the same maximum fidelity well above the  $^2/_3$  needed to confirm quantum entanglement.  $^{21}$  Data sets 2 and 3 show

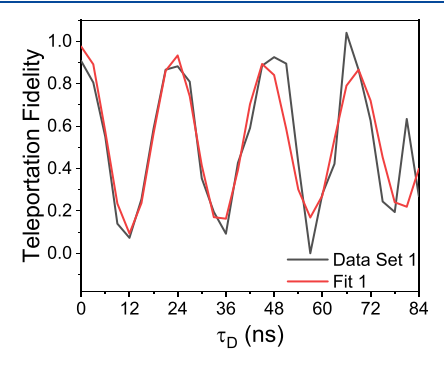


Figure 6. Teleportation fidelity calculated as a function of  $\tau_D$  for data set 1 with a corresponding fit.

similar oscillatory behavior, only with shallower troughs after the trough at around  $\tau_{\rm D}=12$  ns (see the Supporting Information).

The QST as a function of  $\tau_D$  has three main features: (1) oscillatory behavior of the echo intensity, (2) damping of the signal intensity as  $\tau_D$  is increased, and (3) the movement of the echo closer in time to the  $\pi$  microwave pulse at longer  $\tau_D$  values.

The oscillation of the spin echo can be understood in the context of the evolution of the density matrix. The spin state evolves under two different spin Hamiltonians, resulting in the accumulation of a phase equal to their frequency difference. The experimentally obtained frequency of 42.2  $\pm$  0.7 MHz agrees well with the frequency difference of the microwave pulses (40 MHz) used to target R $^{\bullet}$  and D $^{\bullet+}$  and is in good agreement with the average oscillation frequency of the simulated data, 42.2 MHz.

The 38 ns experimental echo decay lifetime is much shorter than the previously reported phase memory time of  $D^{\bullet+}$  ( $T_m = 890$  ns). <sup>12</sup> However, the decay is reproduced quite well in the density matrix simulation and can be interpreted as resulting from spectral diffusion. Initially, the spins dephase due to the magnetic environment of  $R^{\bullet}$ , following teleportation of the spin states to  $D^{\bullet+}$ , where they continue to dephase, but now the spins are in a different magnetic environment and do so in an uncorrelated fashion. The  $\pi$  microwave pulse is unable to completely refocus the coherence, and the spin echo is damped due to destructive interference from the dephasing caused by two different magnetic environments.

This mechanism is fully supported by the density matrix simulation, with an average damping lifetime of 35.6 ns. The simulation does not consider any  $T_{\mathrm{m}}$  relaxation, and the damping is due solely to the two uncorrelated dephasing processes. If the dephasing occurs in a correlated fashion, i.e., dephasing of R<sup>o</sup> occurs with a given frequency offset and continues with the same offset after teleportation to D<sup>•+</sup>, then the echo amplitude does not decrease as a function of  $\tau_D$ . This understanding provides clues about how this teleportation experiment could be made more robust to avoid this particular mechanism of dephasing; for example, rather than the initiation of teleportation immediately following the generation of the quantum state, a Carr-Purcell-Meiboom-Gill<sup>22,23</sup> pulse train could first be applied to the prepared spin state on R to refocus its spin echo prior to application of the laser pulse that initiates teleportation.

The observation that the spin echo moves closer in time to the  $\pi$  pulse with an increase in  $\tau_{\rm D}$  can be explained by considering the time period just before and after the laser pulse that initiates teleportation. The prepared spin state of R<sup>o</sup> evolves initially under its spin Hamiltonian and then dephases under the spin Hamiltonian of D<sup>•+</sup> after the laser pulse occurs at  $\tau_D$ . As a result, the spin ensemble of R $^{\bullet}$  prior to the laser pulse cannot be refocused completely following teleportation. This process is somewhat analogous to decreasing the time between the microwave pulses in a Hahn echo sequence; only here it is the time between the laser pulse and the  $\pi$  pulse, which determines when the echo will appear. Because the time between the microwave pulses is fixed in the experiment, the time at which the spin echo of  $D^{\bullet+}$  appears also changes as  $\tau_D$ changes. This is somewhat analogous to varying the time between the  $\pi/2$  and  $\pi$  pulses in a standard Hahn echo experiment, so that the echo should appear at  $\tau - \tau_D$  after the  $\pi$  microwave pulse. By fitting the maxima and minima in the

echo intensity, we find the average slope of the linear fit is  $-0.70 \pm 0.10$  with an average intercept of 165  $\pm$  5 ns. These values are close to the ideal situation for these experimental conditions, where the slope should be -1 and the y intercept should be 150 ns. Analyzing the corresponding fit lines to each two-dimensional simulated data set, we find the average slope is -1.019 and the average intercept is 201 ns. The difference between the intercepts of the experimental and simulated data is due to the microwave resonator dead time. Because the simulations are not subject to the resonator dead time, the simulated echo data begin directly after the  $\pi$  microwave pulse and are not delayed. The simulated fits show good agreement with the idealized situation, giving credence to the argument that the echo moves closer to the  $\pi$  microwave pulse with an increase in  $\tau_{\rm D}$  analogous to adjusting the time delay between Hahn echo microwave pulses. Overall, the high level of agreement between the experimental data and simulations suggests that our approach to the density matrix evolution can serve as a predictive model for exploring other pulse sequences and protocols for spin teleportation experiments.

In the three-pulse teleportation experiment, only a very weak signal is present. This is the desired outcome as this experiment measures  $\langle S_z \rangle$ , and with properly calibrated turning angles, all of the spins should be in the x-y plane. While no interesting dynamics occur in this experiment, it is nevertheless necessary to collect these data to calculate the fidelity.

As shown in Figure 6 (and Figure S6), the teleportation fidelity oscillates as a function of  $\tau_{\rm D}$ . The fidelity plots might, at first glance, appear to suggest that the system is not teleporting when  $\tau_{\rm D}$  is in a trough as  $F_{\rm teleport}$  is less than the value of  $^2/_3$  required to confirm quantum teleportation. In a manner of speaking that is true, the initially prepared state is not perfectly teleported; it is however teleported with an additional phase factor related to the difference between the spin Hamiltonians and  $\tau_{\rm D}$ , i.e., the oscillation frequency of the spin echo. Fitting the fidelity oscillation gives an average frequency of 41  $\pm$  2 MHz, which, not surprisingly, agrees very well with the oscillation frequency of the observed spin echo.

This study examined the effects of changing the interval between producing a particular spin state on a stable radical and initiating the quantum measurement event, in this case the laser-driven electron transfer, on electron spin state teleportation in a D-A-R molecule. The two-pulse teleportation experiment as a function of  $\tau_{\rm D}$  showed a damped oscillation of the teleported spin echo. A density matrix model was used to simulate these results and provide the insight necessary to understand the spin echo behavior. The teleportation fidelity calculations show oscillations as a function of  $\tau_{\rm D}$  due to the accumulation of a phase factor between  $\langle S_x \rangle$  and  $\langle S_v \rangle$ . Overall, these investigations elucidate how spin state evolution and the ability to control it by varying the input of both optical and microwave pulses into the system can enhance the observation and leveraging of teleportation in molecular systems for QIS applications.

## ASSOCIATED CONTENT

## **Solution** Supporting Information

The Supporting Information is available free of charge at https://pubs.acs.org/doi/10.1021/acs.jpclett.1c03780.

Additional data and processing details about the teleportation laser experiments, simulations, and fidelity

calculations and experimental instrument parameters for each data set (PDF)

#### AUTHOR INFORMATION

### **Corresponding Authors**

Michael R. Wasielewski — Department of Chemistry, Center for Molecular Quantum Transduction, and Institute for Sustainability and Energy at Northwestern, Northwestern University, Evanston, Illinois 60208-3113, United States; orcid.org/0000-0003-2920-5440; Email: m-wasielewski@northwestern.edu

Matthew D. Krzyaniak — Department of Chemistry, Center for Molecular Quantum Transduction, and Institute for Sustainability and Energy at Northwestern, Northwestern University, Evanston, Illinois 60208-3113, United States; orcid.org/0000-0002-8761-7323; Email: mdkrzyaniak@northwestern.edu

#### **Authors**

Laura Bancroft — Department of Chemistry, Center for Molecular Quantum Transduction, and Institute for Sustainability and Energy at Northwestern, Northwestern University, Evanston, Illinois 60208-3113, United States; orcid.org/0000-0002-4312-9758

Yunfan Qiu – Department of Chemistry, Center for Molecular Quantum Transduction, and Institute for Sustainability and Energy at Northwestern, Northwestern University, Evanston, Illinois 60208-3113, United States

Complete contact information is available at: https://pubs.acs.org/10.1021/acs.jpclett.1c03780

#### Notes

The authors declare no competing financial interest.

#### ACKNOWLEDGMENTS

Experimental work was supported by the National Science Foundation under Award CHE-1900422. Theory and simulations were supported as part of the Center for Molecular Quantum Transduction (CMQT), an Energy Frontier Research Center funded by the U.S. Department of Energy, Office of Science, Basic Energy Sciences, under Award DE-SC0021314. The authors thank Jonathan D. Schultz for his help with MATLAB coding.

# REFERENCES

- (1) Pirandola, S.; Eisert, J.; Weedbrook, C.; Furusawa, A.; Braunstein, S. L. Advances in quantum teleportation. *Nat. Photonics* **2015**, *9*, 641–652.
- (2) Bennett, C. H.; Brassard, G.; Crépeau, C.; Jozsa, R.; Peres, A.; Wootters, W. K. Teleporting an unknown quantum state via dual classical and Einstein-Podolsky-Rosen channels. *Phys. Rev. Lett.* **1993**, 70, 1895–1899.
- (3) Bouwmeester, D.; Pan, J.-W.; Mattle, K.; Eibl, M.; Weinfurter, H.; Zeilinger, A. Experimental quantum teleportation. *Nature* **1997**, 390, 575–579.
- (4) Boschi, D.; Branca, S.; De Martini, F.; Hardy, L.; Popescu, S. Experimental realization of teleporting an unknown pure quantum state via dual classical and Einstein-Podolsky-Rosen channels. *Phys. Rev. Lett.* **1998**, *80*, 1121–1125.
- (5) Barrett, M. D.; Chiaverini, J.; Schaetz, T.; Britton, J.; Itano, W. M.; Jost, J. D.; Knill, E.; Langer, C.; Leibfried, D.; Ozeri, R.; et al. Deterministic quantum teleportation of atomic qubits. *Nature* **2004**, 429, 737–739.

- (6) Riebe, M.; Häffner, H.; Roos, C. F.; Hänsel, W.; Benhelm, J.; Lancaster, G. P. T.; Körber, T. W.; Becher, C.; Schmidt-Kaler, F.; James, D. F. V.; et al. Deterministic quantum teleportation with atoms. *Nature* **2004**, *429*, 734–737.
- (7) Sherson, J. F.; Krauter, H.; Olsson, R. K.; Julsgaard, B.; Hammerer, K.; Cirac, I.; Polzik, E. S. Quantum teleportation between light and matter. *Nature* **2006**, *443*, 557–560.
- (8) Steffen, L.; Salathe, Y.; Oppliger, M.; Kurpiers, P.; Baur, M.; Lang, C.; Eichler, C.; Puebla-Hellmann, G.; Fedorov, A.; Wallraff, A. Deterministic quantum teleportation with feed-forward in a solid state system. *Nature* **2013**, *500*, 319–324.
- (9) Nielsen, M. A.; Knill, E.; Laflamme, R. Complete quantum teleportation using nuclear magnetic resonance. *Nature* **1998**, 396, 52–55.
- (10) Gao, W. B.; Fallahi, P.; Togan, E.; Delteil, A.; Chin, Y. S.; Miguel-Sanchez, J.; Imamoglu, A. Quantum teleportation from a propagating photon to a solid-state spin qubit. *Nat. Commun.* **2013**, *4*, 2744.
- (11) Pfaff, W.; Hensen, B. J.; Bernien, H.; van Dam, S. B.; Blok, M. S.; Taminiau, T. H.; Tiggelman, M. J.; Schouten, R. N.; Markham, M.; Twitchen, D. J.; et al. Unconditional quantum teleportation between distant solid-state quantum bits. *Science* **2014**, *345*, 532–535.
- (12) Rugg, B. K.; Krzyaniak, M. D.; Phelan, B. T.; Ratner, M. A.; Young, R. M.; Wasielewski, M. R. Photodriven quantum teleportation of an electron spin state in a covalent donor-acceptor-radical system. *Nat. Chem.* **2019**, *11*, 981–986.
- (13) Nielsen, M. A.; Chuang, I. L. Quantum computation and quantum information; Cambridge University Press: Cambridge, U.K., 2000; pp 702.
- (14) Kandrashkin, Y. E.; Salikhov, K. M. Numerical simulation of quantum teleportation across biological membrane in photosynthetic reaction centers. *Appl. Magn. Reson.* **2010**, *37*, 549–566.
- (15) Salikhov, K. M.; Golbeck, J. H.; Stehlik, D. Quantum teleportation across a biological membrane by means of correlated spin pair dynamics in photosynthetic reaction centers. *Appl. Magn. Reson.* **2007**, *31*, 237–252.
- (16) Kandrashkin, Y. E. Influence of spin decoherence on the yield of photodriven quantum teleportation in molecular triads. *J. Phys. Chem. Lett.* **2021**, *12*, 6405–6410.
- (17) Rugg, B. K.; Phelan, B. T.; Horwitz, N. E.; Young, R. M.; Krzyaniak, M. D.; Ratner, M. A.; Wasielewski, M. R. Spin-selective photoreduction of a stable radical within a covalent donor—acceptor—radical triad. *J. Am. Chem. Soc.* **2017**, *139*, 15660—15663.
- (18) Brenner, M. H.; Cai, D.; Swanson, J. A.; Ogilvie, J. P. Two-photon imaging of multiple fluorescent proteins by phase-shaping and linear unmixing with a single broadband laser. *Opt. Express* **2013**, *21*, 17256.
- (19) Stoll, S.; Schweiger, A. Easyspin, a comprehensive software package for spectral simulation and analysis in EPR. *J. Magn. Reson.* **2006**, *178*, 42–55.
- (20) Gilchrist, A.; Langford, N. K.; Nielsen, M. A. Distance measures to compare real and ideal quantum processes. *Phys. Rev. A* **2005**, *71*, 062310.
- (21) Grosshans, F.; Grangier, P. Quantum cloning and teleportation criteria for continuous quantum variables. *Phys. Rev. A* **2001**, *64*, 010301.
- (22) Carr, H. Y.; Purcell, E. M. Effects of diffusion on free precession in nuclear magnetic resonance experiments. *Phys. Rev.* **1954**, *94*, 630–638.
- (23) Meiboom, S.; Gill, D. Modified spin-echo method for measuring nuclear relaxation times. *Rev. Sci. Instrum.* **1958**, 29, 688–691.